# Space-Time Thermal Binary Coding by a Spatiotemporally Modulated Metashell

Fubao Yang,[1] Peng Jin,[1] Min Lei,[1] Gaole Dai,[2] Jun Wang,[3,4,*] and Jiping Huang[1,†]

[1] *Department of Physics, State Key Laboratory of Surface Physics, and Key Laboratory of Micro and Nano Photonic Structures (MOE), Fudan University, Shanghai 200438, China*

[2] *School of Sciences, Nantong University, Nantong 226019, China*

[3] *School of Physics, East China University of Science and Technology, Shanghai 200237, China*

[4] *School of Mathematics, East China University of Science and Technology, Shanghai 200237, China*

(Received 20 November 2022; revised 9 February 2023; accepted 4 May 2023; published 31 May 2023)

The recently proposed space-time-coding electromagnetic metasurface introduces the temporal dimension into artificial structure design, greatly expanding its digital application in information processing. However, the counterpart in thermal digital metamaterial is still lacking but compelling because the absence of temporal dimension prohibits synergetic modulation of thermal signal in time and space, thus limiting the capacity of information storage and the efficiency of information transmission with heat. Here, we introduce the temporal modulation into existing spatially variable thermal coding structures and propose a space-time thermal binary coding scheme. We design a category of coding units with time-dependent metashells so that they can switch their functionalities between cloaking and concentrating in time sequences. Integrating these identical units on a two-dimensional spatial array, we numerically show that this single metasurface can output various digital signal sequences composed of 0 and 1 in time and space dimensions. We further experimentally realize the temporal modulation with a rotatable concentric multilayered structure driven by a time-stepping motor. These results demonstrate a practical space-time strategy for thermal binary coding, provide a feasible prototype for spatiotemporal regulation of thermal signal, and promisingly open an alternative way for realizing information processing in diffusion systems.

DOI: 10.1103/PhysRevApplied.19.054096

## I. INTRODUCTION

Metamaterials have superior physical properties beyond natural materials because their microstructures and corresponding functions can be artificially designed and tailored [1,2]. The past decades have witnessed the magnificent development of this field covering both wave and diffusion systems, which is still the frontier crossing physics and engineering to date [3–5]. Due to the remarkable machinability and controllability of metamaterials, various unprecedented devices have been presented [6]. Notably, information metamaterials [7,8] are a representative category of advanced applications by digitally regulating electromagnetic wave, and have been particularly significant and promising with the arrival of the big data era. By designing two unit structures with opposite reflection phases as the binary data bits "1" and "0" [9], the proposed digital coding and programmable metamaterials make people accessible to the tools that are similar to electronic computers for processing and storing information. Thus, it provides a different opportunity to bridge the digital and physical worlds beyond existing electron-based computer schemes [10,11]. However, the earlier studies of information metamaterials are almost confined to passive modulation, whose functionalities are fixed in time and tuned only by additional installations. The lack of intelligence and flexibility severely limits their practical application. Fortunately, the recently emerged concept of space time in material design makes it possible to modulate intrinsic functionalities dynamically [12]. The introduction of temporal dimension facilitates space-time-coding digital metasurfaces [13–15], which improves the intelligence and flexibility significantly. Besides wave systems like electromagnetic and acoustic wave, heat transfer is a process of energy diffusion that is ubiquitous in nature. If such a diffusion process can also be utilized to achieve information coding, massive amounts of waste heat will have other application scenarios and it is possible to open an alternative way in diffusion systems for realizing analogy developments of information metamaterials.

Thermal metamaterials provide us with this opportunity to achieve thermal coding by elaborately designing and constructing artificial systems. Thanks to transformation

*wj21@ecust.edu.cn

†jphuang@fudan.edu.cn

 

thermotics [16,17], various thermal metadevices are successfully realized, such as thermal cloaks, concentrators, and rotators [18–20]. Remarkably, a thermal concentrator gathers heat flow while a thermal cloak shields heat flow in their function regions, so that the local heat fluxes of them are completely different under the same boundary conditions. By coding the heat fluxes in the center of thermal cloak and concentrator equivalently as the digital data bits "0" and "1", the concept of binary thermal coding has been proposed [21]. Subsequently, the modulation methods of thermal coding are promptly developed by employing various modes of heat transfer [22,23] and multiple ways of functionality switch [24–27]. However, in the existing works, thermal parameters of coding elements are all fixed in time, saying the exploration of their temporal dimension is intrinsically elusive. Therefore, as previously mentioned, the lack of time sequence seriously reduces the capacity of information storage and the efficiency of information transmission in practical applications.

To solve this problem, in this paper, we propose a space-time thermal binary coding scheme. Inspired by the concept of spatiotemporal modulation on thermal parameters [28–32], we successfully realize united space-time regulation of thermal signal on a single metasurface. The schematic diagram is shown in Fig. 1. Coding unit consists of a spatiotemporally volatile metashell and is arranged in a fixed background. Hot and cold sources are applied to the upper and lower boundaries for thermal signal input, and a probe is placed in the center of every coding unit to detect local heat flux. As the metashell parameters change over time, the coding unit switches between concentrator and cloak accordingly. Thus, the detected heat flux has two states, which can be coded as data bits "1" and "0," corresponding to thermal concentrator and cloak, respectively. The detected heat flux is time varying and space distributing, which can be read out in a space-time sequence. One can integrate coding units into an array metasurface, and program output signal sequences with a field-programmable gate array (FPGA) to store or process thermal information. By recording the time-varying heat flux of every unit and coding them as binary number arrays, space-time coding sequences can be obtained. It means that a single thermal metasurface can output a variety of coding sequences in time and space dimensions, which enhances the information storage and transmission efficiency. Compared with the existing thermal coding metasurfaces, our scheme explores the temporal dimension by spatiotemporal modulation and dramatically improves flexibility and intelligence, hence laying a solid foundation for future practical application. In what follows, we explain the proposed theory in detail, and perform finite-element simulations to validate our theory. Subsequently, we experimentally demonstrate the feasibility of spatiotemporal coding unit. Let us begin with the theoretical methods.

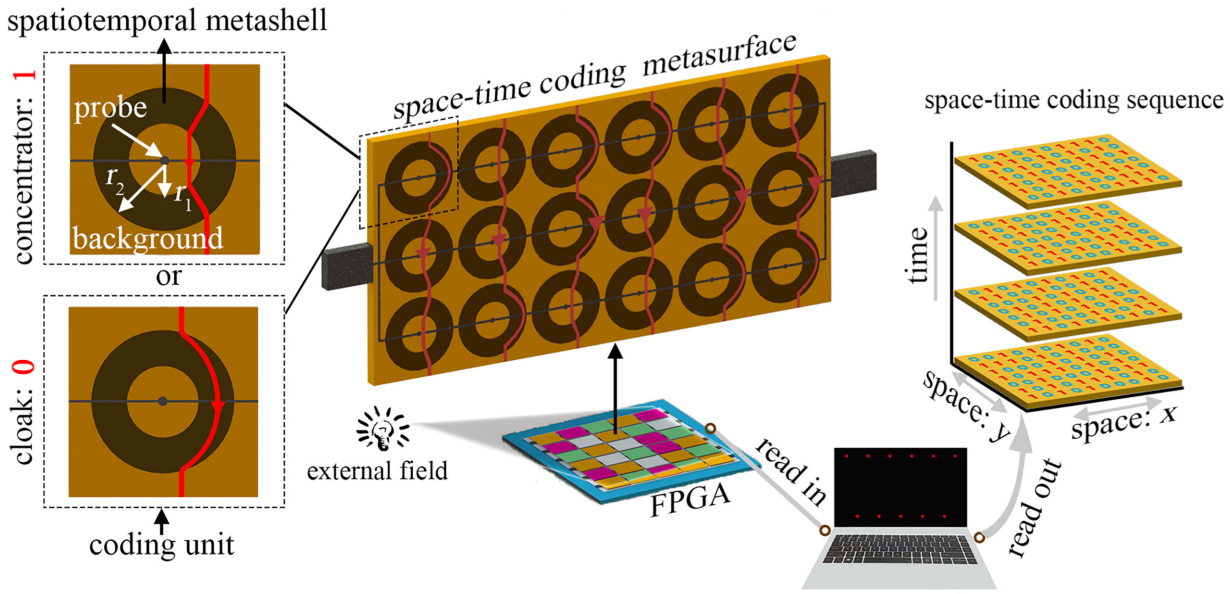


FIG. 1. Conceptual illustration of spatiotemporal thermal binary coding. A probe is placed in the central area of each coding unit to detect the heat flux. The thermal conductivity of the metashell in each coding unit changes over time, causing the unit to switch between concentrator and cloak accordingly. The heat fluxes measured by the probe in these two cases are encoded as equivalent binary data bits 1 and 0. In the illustrated example, many coding units can be integrated into a programmable thermal metasurface, and kinds of this metasurface form a field programmable gate array. Time-varying coding sequences can be obtained by recording the detected heat fluxes and encoding them as binary number arrays.

## II. PRINCIPLE OF SPACE-TIME THERMAL BINARY CODING

Given that heat transfers across the metasurface, the diffusion process without internal heat source is governed by classical Fourier's law

$$\frac{\partial (\rho c T)}{\partial t} + \nabla (-\kappa \nabla T) = 0, \tag{1}$$

where $\rho$, $c$, and $\kappa$ are the mass density, heat capacity, and thermal conductivity, respectively. $T$ is the temperature. Previous studies have proved that Eq. (1) is form invariant under coordinate transformation even though the parameters are spatiotemporally modulated [33], and the transformed parameters satisfy the principle of transformation thermotics, i.e., $\kappa' = J\kappa J^T/\det \mathrm{J}$, $(\rho c)' = \rho c/\det J$, where $\kappa'$ and $(\rho c)'$ are the transformed thermal conductivity and the product of mass density and heat capacity, respectively. In order to avoid the effect of mass flow due to density transformation [30], mass density is set as a constant in this work, and only thermal capacity is transformed. $J$ is Jacobian transformation matrix for coordinate transformation between virtual and physical spaces. Here, we confine heat conduction in the two-dimensional space, so the two-dimensional coordinate transformation is applied. For transformation rules without considering angle in cylindrical coordinates, the Jacobian matrix is $J = \mathrm{diag}(J_r, J_t)$, where $J_r = \partial r'/\partial r$ and $J_t = (r'\partial\theta')/(r\partial\theta) = r'/r$. According to transformation thermotics, the shell ($r_1 < r' < r_2$) parameters of thermal concentrator are [see Part A of the Appendix for detailed derivation]

$$\kappa'_{\mathrm{con}} = \begin{pmatrix} \kappa_0\left(1 - \frac{r_1 - r_3}{r'(r_2 - r_3)} r_2\right) & 0 \\ 0 & \kappa_0 \left(1 - \frac{r_1 - r_3}{r' \cdot (r_2 - r_3)} r_2\right)^{-1} \end{pmatrix}, \tag{2a}$$

$$C'_{\mathrm{con}} = C_0 \left(\frac{r_2 - r_3}{r_2 - r_1}\right)^2 \left(1 - \frac{r_1 - r_3}{r'(r_2 - r_3)} r_2\right), \tag{2b}$$

where $\kappa_0$ and $C_0$ are the thermal conductivity and the product of heat capacity and constant mass density of the background material, and $r_3$ determines the concentrating effect of the central temperature gradient, with a maximum value of $r_2$. $\kappa'_{\mathrm{con}}$ and $C'_{\mathrm{con}}$ represent the transformed shell parameters. The core ($r' < r_1$) parameters are

$$\kappa'_c = \kappa_0, \tag{3a}$$

$$C'_c = C_0 \left(\frac{r_3}{r_1}\right)^2. \tag{3b}$$

Similarly, for thermal cloak, the shell parameters can be derived as [see Part A of the Appendix for detailed derivation]

$$\kappa'_{\mathrm{clo}} = \begin{pmatrix} \kappa_0\left(1 - \frac{\mathrm{r}_1}{r'}\right) & 0 \\ 0 & \kappa\left(1 - \frac{\mathrm{r}_1}{r'}\right)^{-1} \end{pmatrix}, \tag{4a}$$

$$C'_{\mathrm{clo}} = C_0 \left(\frac{\mathrm{r}_2}{\mathrm{r}_2 - \mathrm{r}_1}\right)^2 \frac{r' - \mathrm{r}_1}{r'}, \tag{4b}$$

where $\kappa'_{\mathrm{clo}}$ and $C'_{\mathrm{clo}}$ represent the transformed shell parameters of thermal cloak. Since thermal cloak prevents heat flow into the core, the core parameters can be set arbitrarily without affecting the cloaking function. Comparing Eqs. (2) and (4), it is not hard to see that when $r_3 = 0$, cloak and concentrator share the same shell parameters. Since we hope that the thermal coding unit we propose can switch between cloak and concentrator over time, an appropriate step function needs to be constructed to modulate the shell parameters of a coding unit spatiotemporally.

Herein, we design the spatiotemporal thermal coding unit using a space-time-dependent step function. First, we design the shell parameters of a coding unit as

$$\kappa'_s(x,t) = \begin{pmatrix} \kappa_0\left(1 - \frac{r_1 - r_3 f(t)}{r'(r_2 - r_3 f(t))} r_2\right) & 0 \\ 0 & \kappa_0\left(1 - \frac{r_1 - r_3 f(t)}{r'(r_2 - r_3 f(t))} r_2\right)^{-1} \end{pmatrix}, \tag{5a}$$

$$C'_s(x,t) = C_0 \left(\frac{r_2 - r_3 f(t)}{r_2 - r_1}\right)^2 \left(1 - \frac{r_1 - r_3 f(t)}{r'(r_2 - r_3 f(t))} r_2\right), \tag{5b}$$

where $f(t)$ is the designed time-dependent step function. As $f(t)$ oscillates between 0 and 1 over time, the shell parameters of a coding unit also switch between cloak and concentrator accordingly. The step function $f(t)$ in this work is set as

$$f(t) = \frac{\left(\frac{\cos(\omega t + \phi)}{|\cos(\omega t + \phi)|} + 1\right)}{2}, \tag{6}$$

where $\omega$ is the frequency of the coding unit and $\phi$ is a constant to prevent $\cos(\omega t + \phi)$ from vanishing. As time goes on, $((\cos(\omega t + \phi))/(|\cos(\omega t + \phi)|) + 1)$ oscillates between 0 and 2, so $f(t)$ oscillates between 0 and 1, causing the coding unit to switch between cloak and concentrator. Now, we discuss the core parameters of the coding unit. For thermal cloak, the core parameters can be set arbitrary. For thermal concentrator, the core parameters keep invariant in the steady state according to Eq. (3). Therefore, as shown in Fig. 1, we set the core of the coding unit to the same material as the background. Substituting Eq. (6) into Eq. (5), the parameters of a spatiotemporal coding unit that will switch between cloak and concentrator over time are obtained. Encoding the detected heat fluxes as data bits "0" and "1" when the coding unit

become cloak and concentrator, respectively, we obtain the spatiotemporal thermal binary coding. Then, by integrating such designed coding units into an array, spatiotemporal coding sequences can be output.

A key point to be noted is that the coding sequence is output by programming the heat flux detected in the central region of the coding unit, and the detected heat flux is steady and valid only when the system reaches stable state after switch operation. It means that the system needs to respond instantaneously to rapidly time-varying parameters, which requires the system to be small enough or have a sufficiently large diffusion coefficient. On the other hand, the time for the system to reach steady state should be less than the time period for parameter change in an actual scenario. Otherwise, the detected heat flux is unsteady, which will lead to the coding failure or confusion. Since the output code is meaningful only when the system becomes steady, we can simplify the parameter design of the coding unit to the steady-state case. Thus Eq. (1) can be written as

$$\nabla\,(-\kappa\nabla T) = 0, \tag{7}$$

which indicates the product of heat capacity and constant mass density can be negligible, and only thermal conductivity needs to be considered.

## III. NUMERICAL DEMONSTRATION OF SPATIOTEMPORAL THERMAL BINARY CODING

Numerical demonstration is performed through finite-element simulations with COMSOL Multiphysics [34]. According to above theoretical analysis, we are concerned only about the design of the thermal conductivity of the shell. Directed by Eqs. (5) and (6), three different time-varying coding units with time periods 2, 4, and 6 s are designed by setting $\omega$ as $\pi$, $\pi/2$, and $\pi/3$, respectively. The corresponding simulated temperature fields are shown in Figs. 2(a)–2(c). As previously mentioned, in order to

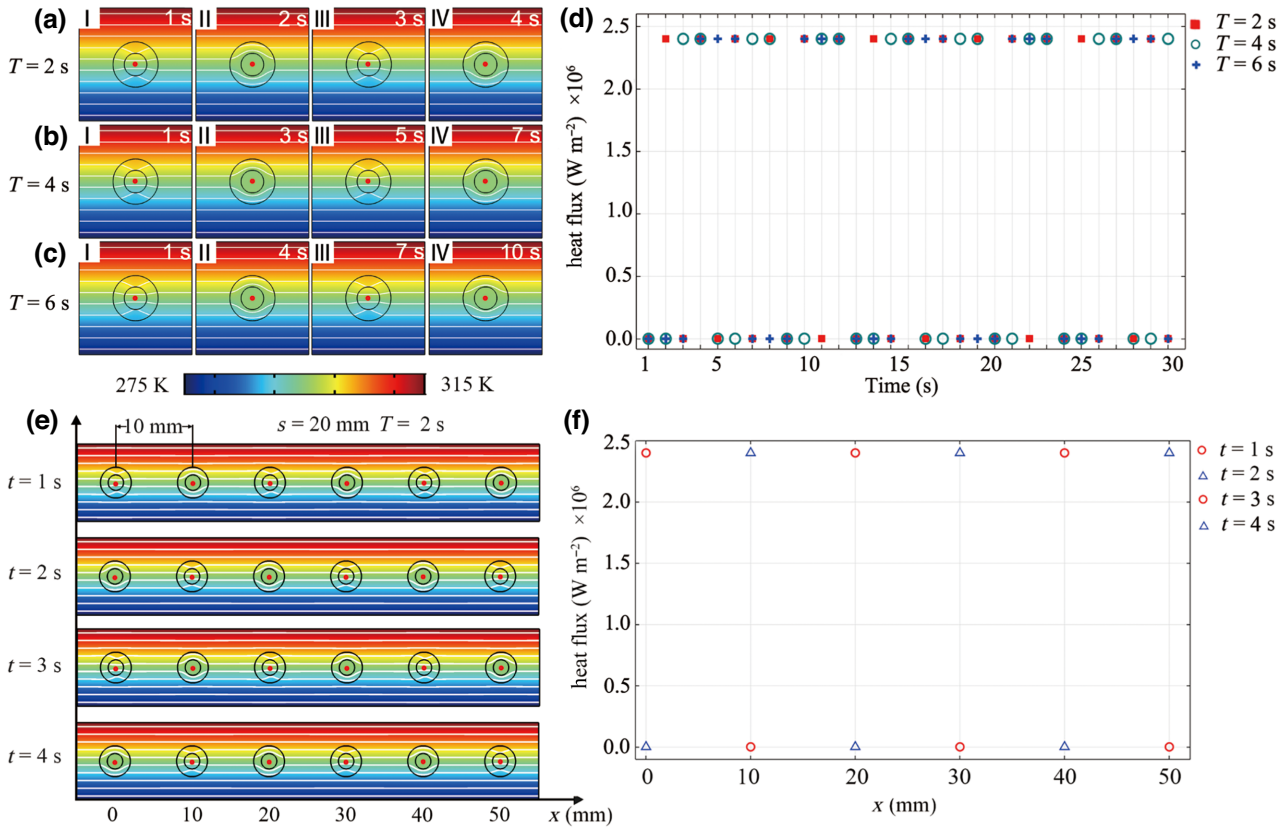


FIG. 2. Simulation results of spatiotemporal thermal binary coding. (a) I–IV are the temperature profiles and isotherms of the coding unit with a time period of 2 s at different times. The coding unit changes from concentrator (or cloak) to cloak (or concentrator) every half a time period. (b),(c) Temperature profiles and isotherms of two coding units with a time period of 4 and 6 s at different times, respectively. Red points in the central region represent probes. (d) Heat fluxes of three coding units detected by probes versus time. The heat fluxes of these three coding units jump between two extremums. These extreme values can be encoded as the binary data bit 1 and 0. (e) Temperature profiles and isotherms at four time points for a coding group integrated by six time-dependent coding units. These coding units have the same time period of 1 s. The space between coding units is 10 mm. (f) Heat fluxes of (e) detected by probes versus spatial distribution. The heat flux switches between maxima and minima every 10 mm, and reverses every 1 s.

ensure that the system can respond instantaneously to rapidly time-varying parameters, the size has to be small enough or the diffusion coefficient is sufficiently large. Accordingly, the side length of the square coding unit is set as 10 mm, and the inner radius $r_1$ and outer radius $r_2$ are 1 and 2 mm, respectively. The background and core are set as coppers with $\kappa_0 = 400\ \mathrm{Wm^{-1}\ K^{-1}}$, $\rho = 8960\ \mathrm{kg\ m^{-3}}$, and $c = 385\ \mathrm{J\ kg^{-1}\ K^{-1}}$. For thermal signal input, the upper and lower sides are fixed at 315 and 275 K. To detect the heat flux in the center of the coding unit, a red point is inserted as a probe. As presented in Figs. 2(a) I–IV, the coding unit with the period of 2 s switches between cloak and concentrator every second. Similar phenomena can be observed in Figs. 2(b) and 2(c). The designed coding unit can switch its function every half period. Figure 2(d) shows the evolution of heat flux over time for three different coding units. We can clearly observe that a jump in heat flux occurs when time passes an integer multiple of the corresponding half-period time. Taking the coding unit with the period of 4 s as an example, when $t = 1, 3, 5, 7, 9$ s, etc., the heat flux jumps. Figures 2(a)–2(d) fully demonstrate the feasibility of spatiotemporal coding units. The detected two heat flux extremes can be encoded as binary data bits "1" and "0". Integrating these coding units at certain spatial intervals, the spatiotemporal coding array is obtained.

We then design a coding group by integrating six coding units with the same time period to demonstrate spatiotemporal thermal coding on a large scale, see Fig. 2(e). The space interval of each unit is 10 mm, and its time period is 2 s. The parameters of all coding units change synchronously, so the time period of the coding group is 2 s, the same as that of each coding unit. We set initial states of these six coding units as concentrator, cloak, concentrator, cloak, concentrator and cloak, respectively. Thus, the initial coding sequence is 101010. Every second, the heat flux of each coding unit jumps, forcing a corresponding change in the coding sequence output by the coding group. The temperature profiles of the group for the first 4 s are shown in Fig. 2(e). We extract the heat-flux data and plot it in Fig. 2(f), which indicates the heat flux versus spatial distribution. Obviously, the heat flux of each coding unit jumps every second, so that the coding group outputs 101010 coding sequence in odd seconds and 010101 in even seconds. The above simulation results imply that the spatiotemporal thermal binary coding with a time period of 2 s and a space period of 20 mm has been successfully implemented.

We further discuss the case where coding units that make up a coding group have different periods. Considering the group designed in Fig. 3, we change the periods for the unit I, II, III, IV, V, and VI to 2, 2, 4, 4, 6, and 6 s, respectively, by setting different $\omega$ according to Eqs. (5)

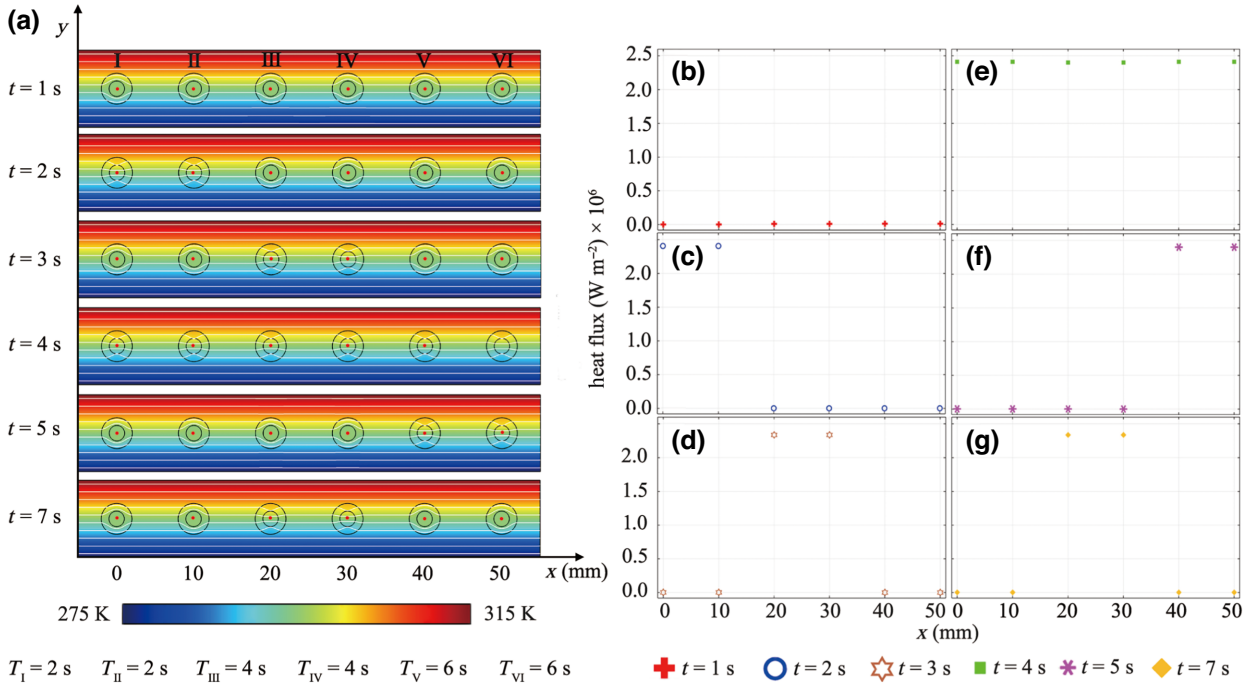


FIG. 3. Simulation results of a coding group integrated by spatiotemporal coding units with different time periods. (a) Temperature profiles and isotherms of the unit group at six time points. The periods of units I, II, III, IV, V, and VI are 2, 2, 4, 4, 6, and 6 s, respectively. The space between coding units is 10 mm. (b)–(g) Heat fluxes of (a) at six time points detected by probes versus spatial location x. The coding group outputs different heat fluxes over time, which can be encoded as time-dependent binary codes.

and (6). The parameters of these coding units change synchronously. It is easy to derive that the period of the group is the least common multiple of the period of all the coding units, equal to 12 s. Figure 3(a) is the temperature profiles of this group at six time points. For coding units I and II, they switch between cloak and concentrator every second. Similarly, units III and IV transition every 2 s, and units V and VI transition every 3 s. The transition time interval is equal to the corresponding half time period of each coding unit. Likewise, Figs. 3(b)–3(g) show the heat fluxes of these six coding units at six time points versus spatial distribution. The initial code is set as 000000. The output code is different at the six time points due to the different periods of each coding unit. Since we know the period of each unit, we can easily infer what coding sequence will be output at some future time point. For example, units I, II, V, and VI are still the cloak at the seventh second because the time has passed by an even multiple of their half-time period. While for units III and IV, they become the concentrator because the past time is equal to an odd multiple of the half-time period. Thus, the detected heat fluxes can be encoded as 001100. To make the time-varying coding group more intuitive, we show the animation of its temperature distributions in Part B of the Appendix, as shown in Video 1. The simulation results show that we can get any code we want at a particular time point by designing the period of each coding unit, which agrees well with the theory.

## IV. EXPERIMENTAL VALIDATION OF SPATIOTEMPORAL THERMAL BINARY CODING

Experimental validation of the time-varying coding unit is carried out and the results are shown in Fig. 4. The spatiotemporal thermal conductivity of the shell is not easy to implement. Here, we overcome this difficulty by an alternative, named tunable doublet metadevices [35], with the spatiotemporal thermal conductivity equivalently

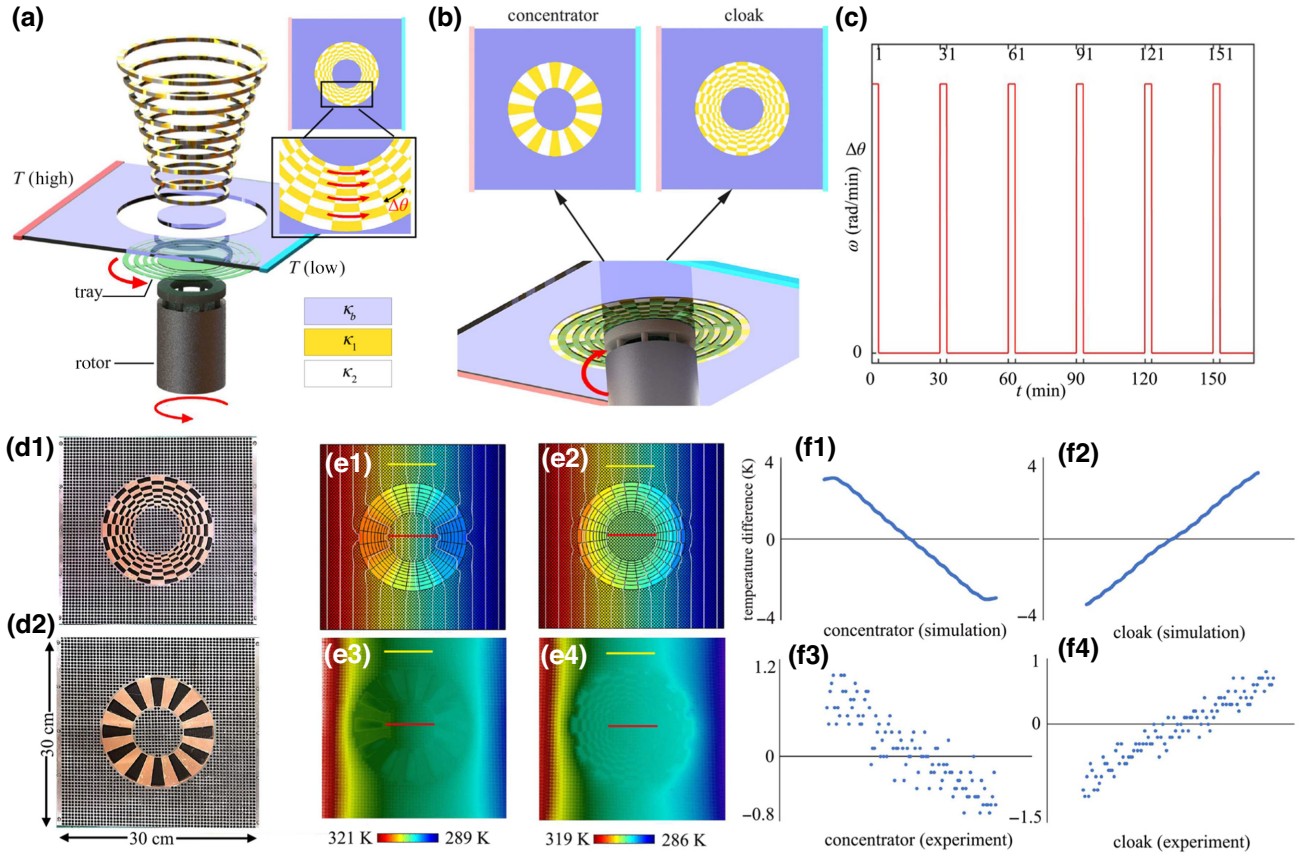


FIG. 4. Experimental demonstration of spatiotemporal thermal coding unit. (a) Experimental setups of the spatiotemporal coding unit. Tunable doublet metadevice is used to equivalently realize the time-varying thermal conductivity. (b) Schematic of the tunable doublet metadevice from the bottom view. The shell configuration switches between the concentrator and cloak as the rotor drives the motion of rings of even layers over time. (c) Diagram of angular velocity versus time of the rotor. (d1),(d2) Actual manufactured spatiotemporal coding units. (d1) A thermal cloak. (d2) A thermal concentrator. (e1),(e2) Numerically simulated temperature fields based on the experimental setup for concentrator and cloak, respectively. (e2),(e3) Experimentally measured temperature fields for concentrator and cloak with an infrared camera. (f1)–(f4) Temperature differences corresponding to (e1)–(e4), which are obtained by subtracting the data of yellow lines from red lines.

replaced by the time-varying structure. Figure 4(a) shows the mechanism of a spatiotemporal thermal coding unit using the tunable doublet metadevice. Its shell consists of nine layers of rings, with each ring divided into 24 fan-shaped unit cells. So the central angle of a unit cell is $\Delta\theta = \pi/12$. Two kinds of isotropic materials with thermal conductivity $\kappa_1$ and $\kappa_2$ are alternately aligned in every ring. The rings of odd layers are fixed and the even ones can be rotated freely. The thermal conductivity of background material is $\kappa_b$. Tunable doublet metadevices require that

$$\sqrt{\kappa_1\kappa_2} = \kappa_b. \tag{8}$$

The detailed derivation can be found in Part A of the Appendix. Equation (8) ensures that the background temperature profile is not distorted by the introduction of the designed shell. We connect a tray at the bottom with rings of even layers and attach the tray to an external rotator. In this way, the tray rotates with the rotor so that rings of even layers will rotate together simultaneously, causing the configuration of the entire shell to change over time. If we arrange the initial shell configuration into the cloak configuration shown in Fig. 4(b), that is, the two materials in the adjacent ring are completely staggered, and input the pulse signal to make the rotor rotates as shown in Fig. 4(c). The even rings will rotate $\Delta\theta$ with the rotor after one pulse period. Then we obtain a structure with the same material aligned along the radial direction, which is the concentrator configuration shown in Fig. 4(b). As the rotor rotates over time under the control of the pulse signal, the shell configuration switches between the concentrator and cloak. Then the spatiotemporal thermal coding unit can be realized by adequately setting the thermal conductivity of these two materials. Therefore, it is feasible to use a time-varying structure to achieve spatiotemporal thermal conductivity equivalently. We choose copper with $\kappa_1 = 400$ W m$^{-1}$ K$^{-1}$ and air with $\kappa_2 = 0.026$ W m$^{-1}$ K$^{-1}$ to form every ring. According to Eq. (8), the thermal conductivity of background material $\kappa_b$ is equal to $\sqrt{\kappa_1\kappa_2} = 3.22$ W m$^{-1}$ K$^{-1}$, which is not common in nature. Here, we realize it with the help of effective medium theory [36,37]. Nickel-chromium iron alloy is used as the substrate, whose thermal conductivity is 9.8 W m$^{-1}$ K$^{-1}$. We fabricate the desired background material based on circle-embedded structures by utilizing laser cutting [38]. The designed circle air holes are uniformly distributed in the background and core, ensuring that the effective thermal conductivity of the corresponding region is equal to 3.22 W m$^{-1}$ K$^{-1}$ [see Part D of the Appendix]. Due to the limited experimental conditions, it is difficult to fabricate coding units with the same size as the simulation system. The actual manufactured coding unit size is 30 × 30 cm, the diameter of the core is 4 cm, and the size parameters of nine rings are confirmed according to the tunable doublet metadevices [35], see Part D of the Appendix for details. Such a large size causes the sample to take nearly 20 min to reach a steady state. Recall that one of the conditions under which the detected heat flux is valid is that the time to steady state is less than that of the parameter switching. Therefore, to meet the above requirements, the period of the pulse signal is set to 30 min, and the time for the continuous input of the excitation signal is set to 1 min, thus the rotor rotates as shown in Fig. 4(c). The coding unit will change its shell structure in 1 min, then re-establish the steady state and output the detected heat flux.

The simulation results of this coding unit in two different configurations are shown in Figs. 4(e1) and 4(e2). It means that the coding unit can switch between concentrator and cloak with the same assembly but different configurations as even rings rotate with the rotor. In the actual experiment, the contact thermal resistance of the rotatable structure composed of nine-layer rings is inevitable due to the limitation of machining technology, resulting in poor experimental results. The scheme is feasible if the thermal contact resistance can be effectively avoided or significantly reduced. To avoid the trouble of contact thermal resistance, two sets of integrated shells are manufactured according to the concentrator and cloak configurations for the demonstration experiment [see Fig. 4(d)]. Figures 4(e3) and 4(e4) are the corresponding experimental results. Because they are two different sets of integrated shells, the temperature boundary conditions are slightly different when conducting the experiment. But this problem will not have any effect on this work. We extract the temperature data at the red lines and yellow lines in Figs. 4(e1)–4(e4). Then we calculate the corresponding temperature differences by subtracting the data of yellow lines from the data of red lines. Figures 4(f1)–4(f4) show the temperature differences corresponding to Figs. 4(e1)–4(e4). It is noted that the experimental results are qualitatively in agreement with the simulation. The detected temperature gradients have two opposite values, which means the heat fluxes in these two samples have two different states. Here, one can conclude that the spatiotemporal thermal coding unit can be achieved with the tunable doublet metadevice, so it is feasible to output time-varying binary coding sequence by encoding the heat flux detected from the coding array integrated by such unit. It is worth noting that there are many ways to modulate thermal conductivity spatiotemporally.

## V. DISCUSSION AND CONCLUSION

In fact, according to the proposed scheme, the period of each unit integrated in the coding array is independently tunable, which means the system can output any coding sequence at any time at will. In addition, the frequency of output time-varying coding sequence depends on the evolution time the system needs to reach steady state. In

order to improve its sensitivity, that is, to output more different coding sequences per unit time, the whole system is required to respond instantaneously to a change in the thermal conductivity. Therefore, the size should be small enough and the diffusion coefficient is large enough, so that the system can reach steady state in an instant, otherwise the heat transfer will get out of whack as the thermal conductivity switches rapidly. Notably, it is not the large the better for the diffusion coefficient due to the consumption of resources. For a medium with diffusion coefficient $\lambda$, the time scale for heat to diffuse over a distance $L$ is $t_s = L^2/t_s$ [39]. To guarantee the detected heat flux is valid, we should ensure that $t_s$ is smaller than the switching interval $t_i$, which requires $\lambda > L^2/t_s$. Therefore, the minimum diffusion coefficient should be bigger than $L^2/t_s$, and we can choose a large diffusion coefficient on the premise of ensuring acceptable resource consumption. For experimental demonstration, the spatiotemporal thermal conductivity is achieved by time-varying structures with the help of tunable doublet metadevices in this work. The enhancement of experimental techniques to reduce the size of coding units can greatly improve the frequency of time-varying thermal coding, so that more different coding sequences can be output per unit time. Notably, there are several other ways to realize the spatiotemporally tuned thermal conductivity, such as by rotatable structure [40–42], electric [43,44], light [45], and fluid [46] modulation.

In conclusion, we propose a space-time thermal binary coding scheme, enabled by spatiotemporally modulating the shell thermal conductivity of coding units. Such coding units can switch between thermal cloak and concentrator over time, so the heat flux in its center has two different states, which can be coded as an equivalently binary data bit 0 and 1. We design time-dependent shell thermal conductivities of coding units and arrange them into a space-distributing array. Coding strategy of the array is verified by numerical simulation. We also conduct a proof-of-principle experiment with the help of tunable doublet metadevices to prove the feasibility of this scheme. Our work introduces the temporal dimension so that a single metasurface can output many different coding sequences, which enhances the information storage and transmission efficiency. Compared with the existing passive digital and programmable thermal metamaterials, this work allows the thermal conductivity of the coding unit to be modulated in real time by the external field, so it improves the intelligence and flexibility by adding time dimension. Because the similar coding behavior also exists in other physical fields, such as mechanics [47,48] and static magnetism [49], our scheme can also extend to these fields. The present works undoubtedly open an alternative way for realizing counterparts of information metamaterials in diffusion systems, and promisingly benefit the digital coding applications such as thermal computing and memory.

## ACKNOWLEDGMENTS

J.-P.H. acknowledges financial support from the National Natural Science Foundation of China under Grant No. 12035004 and from the Science and Technology Commission of Shanghai Municipality under Grant No. 20JC1414700. J.W. acknowledges the financial support from the National Natural Science Foundation of China under Grants No. 12147169 and No. 12205101.

## APPENDIX

### 1. Principle of thermal concentrator, cloak, and tunable doublet metadevices.

1. Principle of thermal concentrator

The schematic diagram of a spatiotemporal coding unit is shown in Fig. 5. The inner and outer radius are $r_1$ and $r_2$, respectively. A thermal concentrator gathers heat flow into the core. So the transformation is to change a larger circular region $r < r_3$ into a small region $r < r_1$ and stretch the region $r_3 < r < r_2$ into region $r_1 < r < r_2$, which can be written as

$$r' = r_1 r/r_c,\ (r < r_3), \tag{A1a}$$

$$r' = \left((r_2 - r_1)\, r + (r_1 - r_3)\, r_2\right) / \left(r_2 - r_3\right),\ (r_3 < r < r_2), \tag{A1b}$$

$$\theta' = \theta, \tag{A1c}$$

where $r'$ is the radius in the transformed space (physical space). According to transformation thermotics, the transformation rules are

$$\kappa' = \frac{J\kappa J^T}{\det J}, \tag{A2a}$$

$$(\rho c)' = \frac{\rho c}{\det J}, \tag{A2b}$$

where $J$ is

$$J = \begin{pmatrix} \frac{\partial r'}{\partial r} & \frac{\partial r'}{(r\partial\theta)} \\ \frac{(r'\partial\theta')}{\partial r} & \frac{(r'\partial\theta')}{(r\partial\theta)} \end{pmatrix}. \tag{A3}$$

According to Eqs. (A1)–(A3), we obtain Eqs. (2) and (3) in the main text.

2. Principle of thermal cloak

A thermal cloak shields heat flow into the core. So the transformation is to compress a circular region $r < r_2$ into a shell region $r_1 < r < r_2$, which can be written as

$$r' = (r_2 - r_1)r/r_2 + r_1,\ (r < r_2), \tag{A4a}$$

$$\theta' = \theta. \tag{A4b}$$

According to Eqs. (A2)–(A4), we obtain Eq. (4) in the main text.

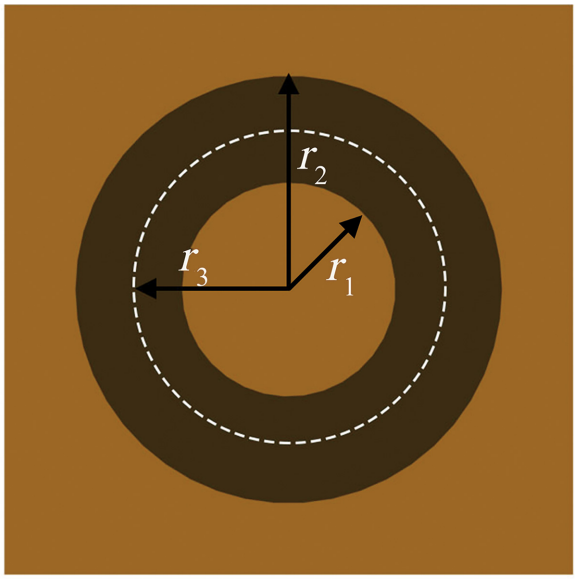


FIG. 5. Schematic diagram of a spatiotemporal coding unit.

3. Principle of tunable doublet metadevices

Equation (8) is derived from Keller's theorem [50]. Keller's theorem calculated the effective conductivity of a two-dimensional two-phase materials and proved that the effective thermal conductivity of a rectangular lattice of identical parallel cylinders is equal to [51]

$$\kappa_x^*(\kappa_1,\kappa_2)\kappa_y^*(\kappa_2,\kappa_1) = \kappa_1\kappa_2, \tag{A5}$$

where $\kappa_x^*(\kappa_1,\kappa_2)$ and $\kappa_y^*(\kappa_2,\kappa_1)$ are the effective thermal conductivities in the $x$ and $y$ directions, respectively. $\kappa_1$ and $\kappa_2$ are the thermal conductivities of two isotropic materials. When the two phases are symmetric, we have $\kappa_x^*(\kappa_1,\kappa_2) = \kappa_y^*(\kappa_2,\kappa_1)$. Thus the corollary of Keller's theorem is obtained, that is,

$$\kappa^*\kappa^* = \kappa_1\kappa_2, \tag{A6}$$

where $\kappa^*$ is the effective thermal conductivity of the two-phase materials. Similarly, in cylindrical coordination, Eq. (A5) is written as

$$\kappa_r^*\kappa_\theta^* = \kappa_1\kappa_2, \tag{A7}$$

where $\kappa_r^*$ and $\kappa_\theta^*$ are the effective thermal conductivities in the radial and tangential directions, respectively. If the two are symmetric, Eq. (A6) also works. To ensure that the background temperature profile is not distorted by the introduction of the two-phase materials, we let $\kappa_b = \kappa^*$, namely

$$\kappa_b = \kappa^* = \sqrt{\kappa_1\kappa_2}, \tag{A8}$$

which is Eq. (8) in the main text.

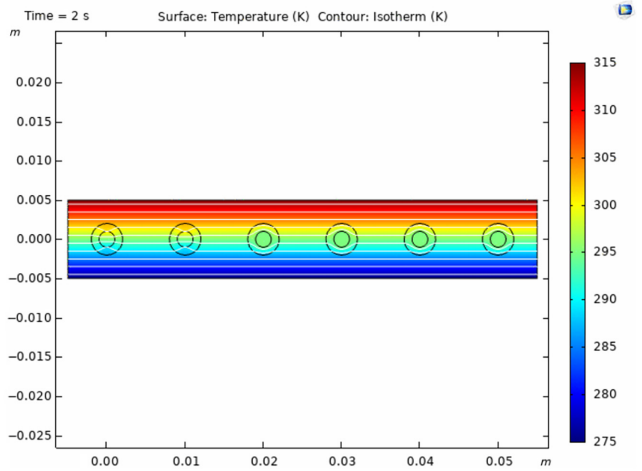


VIDEO 1. Animations for the spatiotemporal thermal coding group in the first 20 s.

### 2. Animations for the spatiotemporal thermal coding group in the first 20 s.

The dynamic thermal parameters of the six metashells in Fig. 3 are calculated according to Eqs. (5) and (6). The periods of units I, II, III, IV, V, and VI are 2, 2, 4, 4, 6, and 6 s by setting $\omega$ equal to $\pi$, $\pi$, $\pi/2$, $\pi/2$, $\pi/3$, and $\pi/3$, respectively. To observe the change of time-varying temperature distribution more clearly, we provide an animation for the first 20 s. See Video 1.

### 3. Numerical details, the mesh-independence study and the time-step-size independence test

1. Numerical details

All numerical simulations of this work are performed in the heat transfer in solids module with COMSOL Multiphysics. We use the time-dependent study, set the study duration to 30 s, and output simulation results per second. The side length of the square coding unit is set as $10^{-2}$ m, and the inner radius $r_1$ and outer radius $r_2$ are $10^{-3}$ m and $2\times10^{-3}$ m, respectively. The background and core are set as coppers with $\kappa_0 = 400$ W m$^{-1}$ K$^{-1}$, $\rho = 8960$ kg m$^{-3}$, and $c = 385$ J kg$^{-1}$ K$^{-1}$. For thermal signal input, the upper and lower sides are set as hot and cold sources, respectively. The shell parameters are calculated by Eq. (5) and (7). With different $\omega$, one can get coding units with different time periods. The numerical mesh parameters used in this work are shown in Table I. Moreover, the time step is taken adaptively by the solver according to the relative tolerance (RT) we set. The relative tolerance in this work is set as 0.001.

2. The mesh-independence study

We perform simulations with the finite-element method, so the mesh-independence study is necessary. All simulations have the same modeling process, but with different

TABLE I. Mesh parameters. Four meshes are adopted in a modeling coding unit for mesh-independence study.

| | Max element size ($m$) | Min element size ($m$) |
|---|---|---|
| Mesh 1 | $3.7 \times 10^{-4}$ | $1.25 \times 10^{-6}$ |
| Mesh 2 | $2 \times 10^{-4}$ | $7.5 \times 10^{-7}$ |
| This work | $1 \times 10^{-4}$ | $2 \times 10^{-7}$ |
| Mesh 3 | $5 \times 10^{-5}$ | $1 \times 10^{-7}$ |

parameters. Therefore, it is sufficient to analyze the independence of only one coding unit. Four different categories of numerical meshes are used to execute an independent study for the designed coding unit with the period of 2 s. The mesh parameters are shown in Table I. Figure 6(a) is the close snapshot of the numerical mesh. We extracted 30 s of data at the position $x = y = 0$ m to compare the results produced by different meshes. See Fig. 6(c). It is noted that the results are mesh independent. Coarser or finer grids give the same result.

3. The time-step-size independence test

In our simulations, the time step is taken adaptively by the solver according to the RT we set. Therefore, four different relative tolerances are taken to test the time-step-size independence. See Fig. 6(d). Relative tolerance is set as 0.001 in this work. Smaller tolerances give more accurate results. It is noted that the results are the same when the relative tolerance becomes smaller. However, the results are unreliable when the relative tolerance is greater than 0.001. We can see that the results are different if the relative tolerance is equal to 0.002. Hence, the simulation results in our work are reliable.

## 4. Experimental details

To avoid or reduce the effect of contact thermal resistance, we manufacture two sets of integrated shells according to the concentrator and cloak configurations for the demonstration experiment. The actual experimental samples are shown in Fig. 4(d). To ensure that the effective thermal conductivity of the background and core is equal to 3.22 W m$^{-1}$ K$^{-1}$, we use circle-embedded structures with nickel-chromium iron alloy as the substrate, whose thermal conductivity is 9.8 W m$^{-1}$ K$^{-1}$. The circle air holes (thermal conductivity is 0.026 W m$^{-1}$ K$^{-1}$) are uniformly distributed in the background and core by utilizing the laser cutting technique. According to the effective medium theory [38], the effective thermal conductivity of the circle-embedded structures $\kappa_e$ is

$$\kappa_e = \kappa_{\mathrm{NC}} \frac{(p + (1-p)L)\kappa_a + (1-p)(1-L)\kappa_{\mathrm{NC}}}{(1-p)L\kappa_a + (p + (1-p)(1-L))\kappa_{\mathrm{NC}}}, \quad \text{(A9)}$$

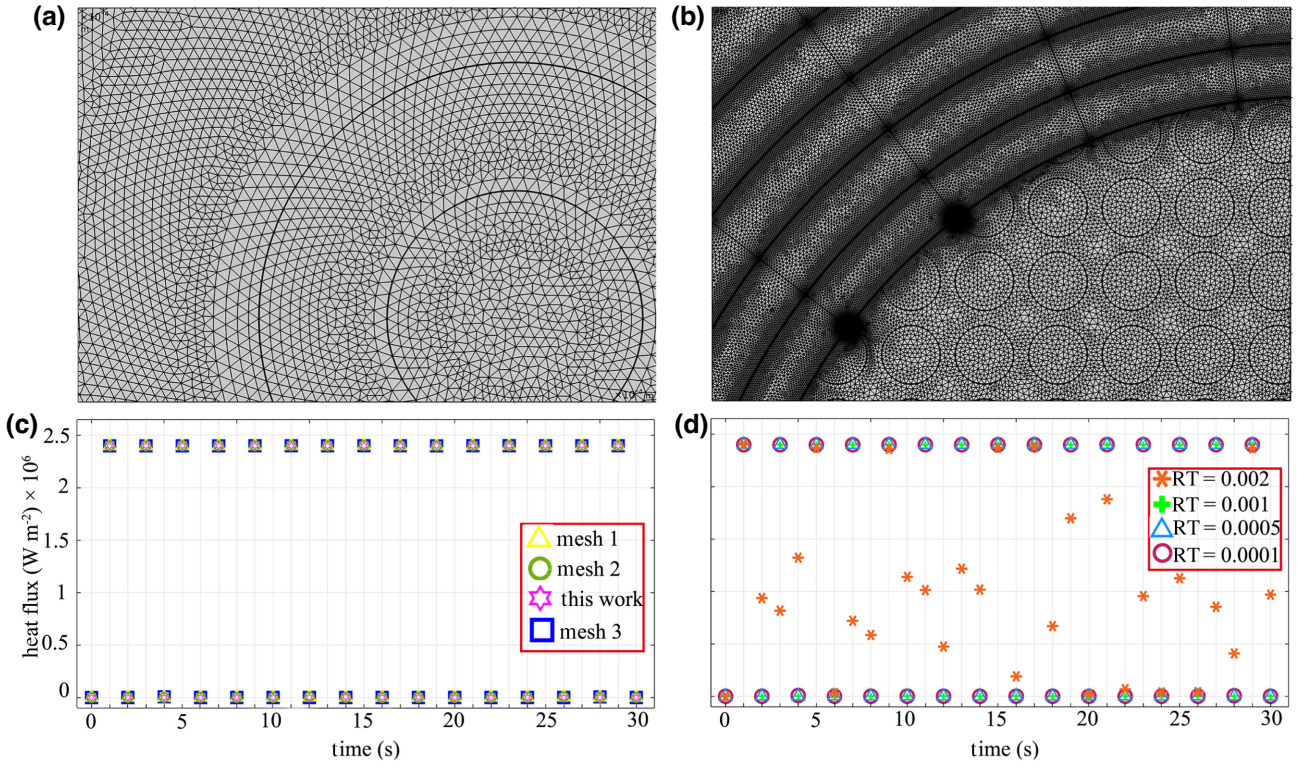


FIG. 6. The mesh-independence study and time-step-size independence test. (a) A close snapshot of the numerical mesh of coding unit. (b) A close snapshot of the numerical mesh of experimental sample. (c) Heat fluxes of the coding unit at the position $x = y = 0$ m with four different meshes. (d) Heat fluxes of the coding unit at the position $x = y = 0$ m with four different relative tolerances.

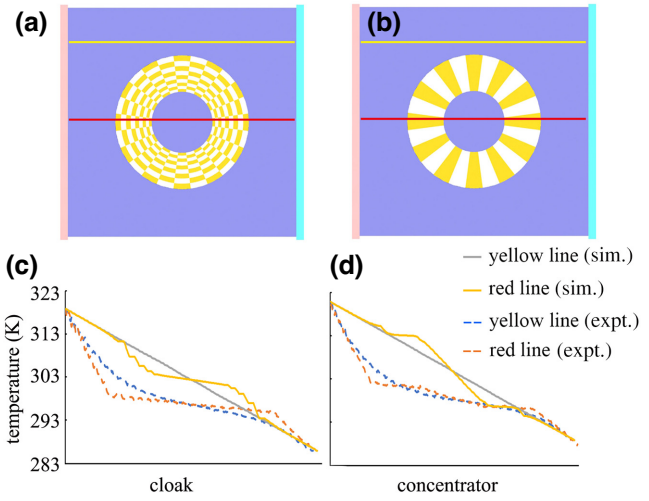


FIG. 7. Comparison of simulation and experimental results. (a) Schematic diagram of simulation and experimental results of cloak. (b) Schematic diagram of simulation and experimental results of concentrator. (c) Comparison of experimental and simulated results of cloak. (d) Comparison of experimental and simulated results of concentrator.

where $\kappa_{\mathrm{NC}}$ and $\kappa_a$ are the thermal conductivity of nickel-chromium iron alloy and air hole, respectively. $p$ is air fraction of the circle-embedded structure. $L$ is the shape factor, which is 1/2 for a circular. Combined with the numerical simulation results, we obtain the radius of each air hole equal to 2 mm. The manufactured coding unit size is $30 \times 30$ cm, the diameter of the core is 4 cm, and the size parameters of nine rings are confirmed according to the tunable doublet metadevices. These nine rings consist of ten circulars, and we use $r_i$ $(i = 1, 2, \ldots, 10)$ to represent the radius of ten circulars, and they should satisfy [35]

$$\ln(r_{i+1}/r_i)/\Delta\theta = \eta, \tag{A10}$$

where $r_1 = 4$ cm, $\Delta\theta = pi/12$, and $\eta$ is a shape parameter. Here, $\eta$ is set as 1/3 so that the coding unit is a thermal cloak when the shell configuration is arranged like Fig. 4(d1) [35]. When the even rings rotate $\Delta\theta$ with the rotor, the shell configuration becomes Fig. 4(d2), which is a thermal concentrator. The radii of ten circulars are 4, 4.3647, 4.7628, 5.1971, 5.671, 6.1881, 6.7524, 7.3681, 8.04, and 8.7737 cm, respectively. The simulation and experimental results of the coding unit are shown in Figs. 4(e1)–4(e2) and Figs. 4(e3)–4(e4) in the main text.

Moreover, we compare the temperature data of experimental and numerical results along the red lines and yellow lines in Fig. 7. Figure 7(a) is a schematic diagram of the simulation and experimental results of the cloak shown in Figs. 4(e2) and 4(e4). Figure 7(b) is a schematic diagram of simulation and experimental results of concentrator shown in Figs. 4(e1) and 4(e3). Figures 7(c) and 7(d) show the simulation and experimental comparisons of cloak and concentrator, respectively. The difference between the experimental and simulation results is due to the effect of air convection, which leads to the overall temperature reduction of the experimental results. However, the experimental results are qualitatively consistent with the simulation results.

[1] V. G. Veselago, The electrodynamics of substances with simultaneously negative values of $\epsilon$ and $\mu$, Sov. Phys. Usp. **10**, 9509 (1968).
[2] J. Pendry, A. Holden, W. Stewart, and I. Youngs, Extremely Low Frequency Plasmons in Metallic Mesostructures, Phys. Rev. Lett. **76**, 47737 (1996).
[3] M. Wegener, Metamaterials beyond optics, Science **342**, 939 (2013).
[4] M. Kadic, T. Bückmann, R. Schittny, and M. Wegener, Metamaterials beyond electromagnetism, Rep. Pro. Phys. **76**, 126501 (2013).
[5] Z. R. Zhang, L. J. Xu, T. Qu, M. Lei, Z.-K. Lin, X. P. Ouyang, J.-H. Jiang, and J. P. Huang, Diffusion metamaterials, Nat. Rev. Phys. **5**, 218 (2023).
[6] N. I. Zhuledev and Y. S. Kivshar, From metamaterials to metadevices, Nat. Mater. **11**, 917 (2012).
[7] X. Fu and T. J. Cui, Recent progress on metamaterials: From effective medium model to real-time information processing system, Pro. Quant. Electron **67**, 100223 (2019).
[8] T. J. Cui, L. L. Lian, L. Shuo, M. Qian, Z. Lei, W. Xiang, X. J. Wei, and C. Qiang, Information metamaterial systems, iScience **23**, 101403 (2020).
[9] T. J. Cui, M. Q. Qi, X. Wan, J. Zhao, and Q. Cheng, Coding metamaterials, digital metamaterials and programmable metamaterials, Light: Sci. Appl. **3**, e218 (2014).
[10] T. J. Cui, S. Liu, and L. L. Li, Information entropy of coding metasurface, Light: Sci. Appl. **5**, e16172 (2016).
[11] T. J. Cui, S. Liu, and L. Zhang, Information metamaterials and metasurfaces, J. Mater. Chem. C **5**, 3644 (2017).
[12] L. Q. Yuan and S. H. Fan, Temporal modulation brings metamaterials into new era, Light: Sci. Appl. **11**, 173 (2022).
[13] J. Y. Dai, J. Zhao, Q. Cheng, and T. J. Cui, Independent control of harmonic amplitudes and phases via a time-domain digital coding metasurface, Light: Sci. Appl. **7**, 1 (2018).
[14] L. Zhang, X. Q. Chen, S. Liu, Q. Zhang, J. Zhao, J. Y. Dai, G. D. Bai, X. Wan, Q. Cheng, G. Castaldi, V. Galdi, and T. J. Cui, Space-time-coding digital metasurfaces, Nat Commun. **9**, 4334 (2018).
[15] C. Liu, Q. Ma, Z. J. Luo, Q. R. Hong, Q. Xiao, H. C. Zhang, L. Miao, W. M. Yu, Q. Cheng, L. L. Li, and T. J. Cui, A programmable diffractive deep neural network based on a digital-coding metasurface array, Nat. Electron. **5**, 113 (2022).
[16] C. Z. Fan, Y. Gao, and J. P. Huang, Shaped graded materials with an apparent negative thermal conductivity, Appl. Phys. Lett. **92**, 251907 (2008).
[17] T. Y. Chen, C.-N. Weng, and J.-S. Chen, Cloak for curvilinearly anisotropic media in conduction, Appl. Phys. Lett. **93**, 114103 (2008).

[18] S. Yang, J. Wang, G. L. Dai, F. B. Yang, and J. P. Huang, Controlling macroscopic heat transfer with thermal metamaterials: Theory, experiment and application, Phys. Rep. **908**, 1 (2021).

[19] Y. Li, W. Li, T. C. Han, X. Zheng, J. X. Li, B. W. Li, S. H. Fan, and C.-W. Qiu, Transforming heat transfer with thermal metamaterials and devices, Nat. Rev. Mater. **6**, 488 (2021).

[20] L. J. Xu and J. P. Huang, *Transformation Thermotics and Extended Theories: Inside and Outside Metamaterials* (Springer, Singapore, 2023).

[21] R. Hu, S. Y. Huang, M. Wang, L. Zhou, X. Peng, and X. Luo, Binary Thermal Encoding by Energy Shielding and Harvesting Units, Phys. Rev. Appl. **10**, 054032 (2018).

[22] J. Shang, B. Y. Tian, C. R. Jiang, and J. P. Huang, Digital thermal metasurface with arbitrary infrared thermogram, Appl. Phys. Lett. **113**, 261902 (2018).

[23] J. Wang, F. B. Yang, L. J. Xu, and J. P. Huang, Omnithermal Restructurable Metasurfaces for Both Infrared-Light Illusion and Visible-Light Similarity, Phys. Rev. Appl. **14**, 014008 (2020).

[24] R. Hu, S. Huang, M. Wang, X. Luo, J. Shiomi, and C.-W. Qiu, Encrypted thermal printing with regionalization transformation, Adv. Mater. **31**, 1807849 (2019).

[25] Z. F. Xu, L. Q. Li, X. C. Chang, Y. Zhao, and W. Y. Wang, Thermal field manipulation via a two-phase thermal metamaterial, Appl. Mater. Today **22**, 10091 (2021).

[26] J. Guo, G. Q. Xu, D. Tian, Z. G. Qu, and C.-W. Qiu, A real-time self-adaptive thermal metasurface, Adv. Mater. **34**, 2201093 (2022).

[27] M. Lei, C. R. Jiang, F. B. Yang, J. Wang, and J. P. Huang, Programmable all-thermal encoding with metamaterials, Int. J. Heat Mass Transfer **207**, 124033 (2023).

[28] D. Torrent, O. Poncelet, and J. C. Batsale, Nonreciprocal Thermal Material by Spatiotemporal Modulation, Phys. Rev. Lett. **120**, 125501 (2018).

[29] C. Y. Hua and L. Lindsay, Space-time dependent thermal conductivity in nonlocal thermal transport, Phys. Rev. B **102**, 104310 (2020).

[30] J. X. Li, Y. Li, P. C. Cao, M. H. Qi, X. Zheng, Y. G. Peng, B. W. Li, X. F. Zhu, A. Alù, H. S. Chen, and C.-W. Qiu, Reciprocity of thermal diffusion in time-modulated systems, Nat. Commun. **13**, 167 (2022).

[31] L. J. Xu, G. Q. Xu, J. P. Huang, and C.-W. Qiu, Diffusive Fizeau Drag in Spatiotemporal Thermal Metamaterials, Phys. Rev. Lett. **128**, 145901 (2022).

[32] L. J. Xu, G. Q. Xu, J. X. Li, Y. Li, J. P. Huang, and C.-W. Qiu, Thermal Willis Coupling in Spatiotemporal Diffusive Metamaterials, Phys. Rev. Lett. **129**, 155901 (2022).

[33] F. B. Yang, L. J. Xu, J. Wang, and J. P. Huang, Transformation Theory for Spatiotemporal Metamaterials, Phys. Rev. Appl. **18**, 034080 (2022).

[34] http://www.comsol.com/.

[35] J. X. Li, Y. Li, T. L. Li, W. Y. Wang, L. Q. Li, and C.-W. Qiu, Doublet Thermal Metadevice, Phys. Rev. Appl. **11**, 044021 (2019).

[36] J. P. Huang and K. W. Yu, Enhanced nonlinear optical responses of materials: Composite effects, Phys. Rep. **431**, 87 (2006).

[37] B. Y. Tian, J. Wang, G. L. Dai, X. P. Ouyang, and J. P. Huang, Thermal metadevices with geometrically anisotropic heterogeneous composites, Int. J. Heat Mass Transfer **174**, 121312 (2021).

[38] S. Yang, L. J. Xu, R. Z. Wang, and J. P. Huang, Full control of heat transfer in single-particle structural materials, Appl. Phys. Lett. **111**, 121908 (2017).

[39] L. R. Glicksman and J. H. Lienhard, *Modelling and Approximation in Heat Transfer* (Cambridge University Press, New York, 2016).

[40] M. Camacho, B. Edwards, and N. Engheta, Achieving asymmetry and trapping in diffusion with spatiotemporal metamaterials, Nat. Commun. **11**, 3733 (2020).

[41] J. X. Li, Y. Li, P.-C. Cao, T. Z. Yang, X.-F. Zhu, W. Y. Wang, and C.-W. Qiu, A continuously tunable solid-like convective thermal metadevice on the reciprocal line, Adv. Mater. **32**, 2003823 (2020).

[42] G. Q. Xu, K. C. Dong, Y. Li, H. G. Li, K. P. Liu, L. Q. Li, J. Q. Wu, and C.-W. Qiu, Tunable analog thermal material, Nat. Commun. **11**, 6028 (2020).

[43] G. Z. Qin, Z. Z. Qin, S.-Y. Yue, Q.-B. Yan, and M. Hu, External electric field driving the ultra-low thermal conductivity of silicene, Nanoscale **9**, 7227 (2017).

[44] S. C. Deng, J. L. Yuan, Y. L. Lin, X. X. Yu, D. K. Ma, Y. W. Huang, R. C. Ji, G. Z. Zhang, and N. Yang, Electric-field induced modulation of thermal conductivity in poly (vinylidene fluoride), Nano Energy **82**, 105749 (2021).

[45] J. Shin, J. Sung, M. Kang, X. Xie, B Lee, K. M. Lee, T. J. White, C. Leal, N. R. Sottos, P. V. Braun, and D. G. Cahill, Light-triggered thermal conductivity switching in azobenzene polymers, Proc. Natl. Acad. Sci. U.S.A. **116**, 5973 (2019).

[46] P. Jin, J. R. Liu, L. J. Xu, J. Wang, X. P. Ouyang, J.-H. Jiang, and J. P. Huang, Light-triggered thermal conductivity switching in azobenzene polymers, Proc. Natl. Acad. Sci. U.S.A. **120**, e2217068120 (2019).

[47] J. P. Udani and A. F. Arrieta, Programmable mechanical metastructures from locally bistable domes, Extreme Mech. Lett. **42**, 101081 (2021).

[48] T. Chen, M. Pauly, and P. M. Reis, A reprogrammable mechanical metamaterial with stable memory, Nature **589**, 386 (2021).

[49] Z. P. Chen, Y. Y. Lin, G. Z. Zheng, Y. W. Yang, Y. X. Zhang, S. Q. Zheng, J. W. Li, J. W. Li, L. Ren, and L. L. Jiang, Programmable transformation and controllable locomotion of magnetoactive soft materials with 3D-patterned magnetization, ACS Appl. Mater. Interfaces **12**, 58179 (2020).

[50] J. B. Keller, A theorem on the conductivity of a composite medium, J. Math. Phys. **5**, 548 (1964).

[51] K. Schulgasser, A reciprocal theorem in two-dimensional heat transfer and its implications, Int. Commun. Heat Mass Transfer **19**, 639 (1992).